



UNIVERSITY OF LEEDS

This is a repository copy of *On a fabric evolution law incorporating the effects of b-value*.

White Rose Research Online URL for this paper:

<http://eprints.whiterose.ac.uk/138165/>

Version: Accepted Version

Article:

Yuan, R, Yu, HS orcid.org/0000-0003-3330-1531, Yang, DS et al. (1 more author) (2019) On a fabric evolution law incorporating the effects of b-value. *Computers and Geotechnics*, 105. pp. 142-154. ISSN 0266-352X

<https://doi.org/10.1016/j.compgeo.2018.09.019>

© 2018 Elsevier Ltd. All rights reserved. Licensed under the Creative Commons Attribution-Non Commercial No Derivatives 4.0 International License (<https://creativecommons.org/licenses/by-nc-nd/4.0/>).

Reuse

This article is distributed under the terms of the Creative Commons Attribution-NonCommercial-NoDerivs (CC BY-NC-ND) licence. This licence only allows you to download this work and share it with others as long as you credit the authors, but you can't change the article in any way or use it commercially. More information and the full terms of the licence here: <https://creativecommons.org/licenses/>

Takedown

If you consider content in White Rose Research Online to be in breach of UK law, please notify us by emailing eprints@whiterose.ac.uk including the URL of the record and the reason for the withdrawal request.



eprints@whiterose.ac.uk
<https://eprints.whiterose.ac.uk/>

1 **On a fabric evolution law incorporating the effects of b-**
2 **value**

3
4 **Dr Ran Yuan**

5 Key Laboratory of High-speed Railway Engineering (Southwest Jiaotong
6 University), Ministry of Education

7 Email: yuanran@swjtu.edu.cn

8 **Professor Hai-Sui YU**

9 School of Civil Engineering,
10 University of Leeds, Leeds LS2 9JT, UK

11 Email: h.yu@leeds.ac.uk

12 **Dr Dun-Shun Yang**

13 Nottingham Centre for Geomechanics,
14 University of Nottingham, Nottingham NG7 2RD, UK

15 Email: dunshun.yang@arup.com

16
17 **Dr Nian Hu**

18 Corresponding author

19 Nottingham Centre for Geomechanics,
20 University of Nottingham, Nottingham NG7 2RD, UK

21 Email: greaterhu@163.com

22

ABSTRACT

23 In this paper, the effects of the intermediate stress ratio, i.e., b-value ($b=(\sigma_2-\sigma_3)/(\sigma_1-\sigma_3)$), on
24 the contact normal-based fabric evolution of granular material, are incorporated into an extant
25 hybrid fabric evolution law. The new evolution law is validated by Discrete Element Method
26 (DEM) simulation results under monotonic shearing with different b-values. Predictions of the
27 proposed generalized fabric evolution law agree well with the DEM simulation results. This
28 evolution law can be widely used for constitutive modelling of granular materials, considering
29 the effects of b-value in a general geomechanical three-dimensional stress space.

30 Keywords: Fabric evolution; Evolution law; Effects of b-value; DEM

31 **1 Introduction**

32 Most field problems in geotechnical engineering, e.g., earthquake, traffic loading, and river
33 embankments, involve a general loading condition ($\sigma_1 \geq \sigma_2 \geq \sigma_3$), where soils are subject to
34 complicated loading paths, together with changes in the magnitudes of the three principal
35 stresses (i.e., σ_1 , σ_2 and σ_3) and rotations of their directions. Real soils, especially sands, are
36 loading path dependent. This means that their behaviours are affected by the magnitudes of the
37 three principal stresses and their directions; hence, it is significant to take all the three principal
38 stresses into consideration in geotechnical engineering design and construction.

39 One interesting aspect of soil response is the sensitivity of the mechanical soil behaviour to the
40 intermediate stress ratio, i.e., b-value. The b-value is introduced as a non-dimensional
41 parameter $b = (\sigma_2 - \sigma_3) / (\sigma_1 - \sigma_3)$, where σ_1 and σ_3 are the major and minor principal stresses,
42 respectively. The b-value is widely used to describe the effects of intermediate principal stress
43 (σ_2), which was first proposed by Habib [1], who performed a series of torsional triaxial tests
44 to investigate the strength characteristics of clays and sands. Bishop [2] determined that the
45 influence of intermediate principal stress σ_2 on soil response can be more readily appreciated
46 in terms of b-value rather than σ_2 itself. In the early 1960s, a number of researchers focused on
47 the study of the effects of the b-value on the soil behaviours, e.g., Bjerrum and Kummeneje [3]
48 and Cornforth [4]. A review of the above work was made by Oda et al [5], who compared
49 triaxial and plane-strain test results and noted that (1) the friction angle in plane strain testing
50 ($b=0.2\sim 0.3$) is up to 10% ~ 20% larger than that in triaxial compression testing ($b=1.0$) for
51 dense sand tested under a low confining pressure and (2) the strain to failure is smaller in plane
52 strain testing ($b=0.2\sim 0.3$) than that in triaxial compression testing ($b=1.0$) for sands of similar
53 densities. It is obvious, from their observations, that the b-value demonstrates significant

54 effects on soil strength and stress-strain behaviours. Similar findings in the experiments were
55 proposed by using various advanced testing apparatuses, e.g., triaxial testing [6-8] and Hollow
56 cylinder testing [9-12]. Recently, DEM simulations have been used to perform cubic triaxial
57 testing (e.g., [13, 14]) and Hollow cylinder testing (e.g., [15, 16]) and demonstrated good
58 consistency with experimental behaviours. These findings in both the laboratory and DEM
59 simulations confirmed and enhanced the conclusions that b -value has significant effects on the
60 deformation and strength behaviour of granular materials, e.g., sands.

61 From micromechanical analysis [17, 18], the effects of b -value on strength are strongly linked
62 to the distribution of the contact normal, hence to the fabric tensor based on the contact normal
63 [19, 20]. For example, the stress-force-fabric relationship suggests that the peak stress ratio is
64 dependent on the contact normal distribution anisotropy [21, 22]. Evidence from DEM
65 simulations has directly demonstrated that peak fabric anisotropy [13, 23] and critical fabric
66 anisotropy [24] are not circular in the deviatoric plane for different b -values. These effects are
67 also confirmed by the DEM simulations carried out by Li et al [15].

68 Several formulations have been proposed to characterize the effects of b -value on the peak and
69 residual strengths of both the initial isotropic and anisotropic granular materials [25-29]. These
70 formulations for constitutive modelling are developed phenomenologically. Indeed,
71 phenomenological models have shown their abilities to capture the macro effects of b -value,
72 the evolution of the internal structure however is ignored in phenomenological models. In
73 addition, those models introduced too many parameters without physical meanings and are
74 difficult for calibration. On the other hand, an increasing interest in microscopic modelling and
75 multi-scale approaches is rising, e.g., fabric-based constitutive modelling. Fabric evolution law,
76 accounting for the microscopic information, is the essential element to develop fabric-based
77 constitutive models for anisotropic behaviours of granular materials. To develop constitutive
78 models considering the effects of b -value as well as anisotropy, the effects of b -value on the

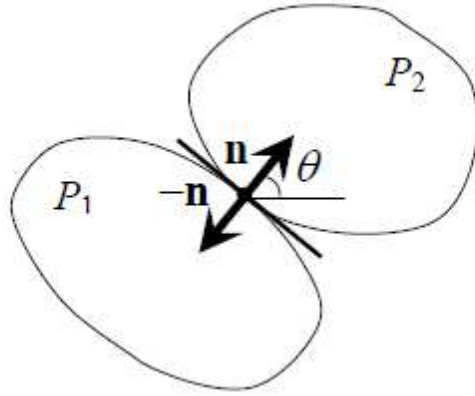
79 fabric evolution law should be considered. Since the sensitivity of the b-value on the
80 mechanical response of the granular materials has been widely identified, many researcher (e.g.,
81 [30, 31]) have tried to incorporate this feature into their three dimensional constitute models.
82 However, the effects of the b-value on the fabric evolution, e.g. the critical stress ratio and the
83 critical fabric anisotropy (as evident above), has not been displayed yet.

84 In this paper, we generalize a hybrid fabric evolution law, which is calibrated with results of
85 fabric evolution statistically obtained from the micro-scale geometrical quantities, to
86 incorporate the effects of b-value on the evolution of fabric. To achieve this, we incorporate
87 the effects of b-value into the proposed hybrid evolution law by assuming that C_1 and C_F are
88 dependent on the b-value in terms of the Lode angle θ_l . The modified evolution law considers
89 both the effects of anisotropy and b-value on the fabric evolution. It can be widely used for
90 fabric-based constitutive modelling of granular materials responding to general stress paths,
91 together with simple isotropic constitutive models, such as the Cam clay Model, Modified Cam
92 clay Model, or the Clay and Sand Model (CASM) proposed by Yu [32, 33]. However, this
93 work is beyond the scope of this paper and will be presented in a future paper.

94 **2 Generalization of the fabric evolution law**

95 2.1 Definitions of fabric tensor

96 As shown in Fig. 1, for each contact point, there are two types of unit contact normal, \mathbf{n} and
97 $-\mathbf{n}$.



98

99

Fig.1 Definition of the contact normal

100 The relative frequency distribution of the contact normal may be described by a probability
 101 density function $\mathbf{E}(\mathbf{n})$. The density function is defined so that it satisfies the following equation:

102
$$\int_{\Omega} E(\mathbf{n}) d\Omega = 1 \quad (1.1)$$

103 where $\Omega = \frac{A}{r^2}$ is a solid angle for the three dimensional space; A denotes the spherical surface
 104 area and r denotes the radius of the considered sphere. Given that each point has two types of
 105 contact normal opposite to each other, we must have:

106
$$E(\mathbf{n}) = E(-\mathbf{n}) \quad (1.2)$$

107 In most cases in three dimensional materials (e.g., [21-22, 35-36]), it can be truncated by
 108 spherical harmonic series in second-order as

109
$$E(\mathbf{n}) = \frac{1}{4\pi} (1 + \mathbf{F} : \mathbf{n} \otimes \mathbf{n}) \quad (1.3)$$

110 The tensor \mathbf{F} in equation (1.3) is known as the second-order fabric tensor of the third kind in
 111 terms of unit contact normal. Fabric tensor \mathbf{F} is traceless, and can be used to describe the fabric
 112 anisotropy in the assembly.

113 Practically, the tensor \mathbf{F} can be estimated from the second-order fabric tensor \mathbf{N} as follows (e.g,
 114 [21, 34, 36-37]):

115
$$\mathbf{F} = \frac{15}{2} \left(\mathbf{N} - \frac{1}{3} \mathbf{I} \right) \quad (1.4)$$

116 where \mathbf{N} can be determined from the discrete directional contact normal \mathbf{n} of a granular
 117 assembly by

118
$$\mathbf{N} = \frac{1}{N_c} \sum_{c \in N_c} \mathbf{n}^c \otimes \mathbf{n}^c \quad (1.5)$$

119 2.2 Fabric tensor at a critical state

120 Granular materials under monotonic shearing will achieve a critical state characterised by
 121 stationary values of stress, void ratio with the unlimited development of shear strain [38-41].
 122 We redefine the anisotropic fabric state by adding one more equation which enables a
 123 requirement on fabric tensor at the critical state (critical fabric tensor) into the conventional
 124 definition of the critical state. The critical fabric tensor \mathbf{F}_c is assumed to be proportional with
 125 the deviatoric stress ratio tensor $\boldsymbol{\eta}$ at the critical state, i.e.

126
$$\mathbf{F}_c = C_F(b) \boldsymbol{\eta}_c = C_F(b) \left(\frac{\mathbf{S}}{p} \right)_c \quad (1.6)$$

127 where C_F is a proportional coefficient generally dependent on the b -value, $\eta_c = \sqrt{3/2} \|\boldsymbol{\eta}\|$, \mathbf{s}
 128 is the stress deviator and p is the mean effective stress.

129 The spatial distribution of contact normal keeps evolving to support the mobilised strength.
 130 The rate of the fabric, i.e., $\dot{\mathbf{F}}$, is characterized by the fabric evolution law; hence the physical
 131 description of the rate of the fabric is defined as the changing of the spatial distribution of
 132 contact normal. In this paper, a hybrid fabric evolution law has been proposed based on the
 133 principle of material frame indifference, with the assumption of rate-independency and unique
 134 critical fabric state, i.e.,

135
$$\dot{\mathbf{F}} = C_1(1 + C_2 \|\boldsymbol{\eta}\|) \dot{\boldsymbol{\eta}} + C_3 \dot{\Lambda} (C_F \boldsymbol{\eta} - \mathbf{F}) \quad (2.1)$$

136
$$C_F = \left(\frac{F_q}{\eta} \right)_c, F_q = \sqrt{3/2} \|\mathbf{F}\|, \eta = \sqrt{3/2} \|\boldsymbol{\eta}\| \quad (2.2)$$

137 where C_1, C_2, C_3 are material constants controlling the rate of fabric tensor, hence the
 138 microscopic mechanisms of the fabric evolution; $\boldsymbol{\eta} = \mathbf{S}/p$ is a stress ratio tensor representing
 139 the deviatoric stress tensor \mathbf{S} normalized by the mean stress p ; $\dot{\Lambda}$ is a norm of rate of the
 140 deviatoric plastic strain, i.e., $\dot{\Lambda} = \|\dot{\epsilon}_p\|$; F_q determines the fabric deviator.

141 It is postulated in the evolution law that the rate of the fabric tensor, which is defined on the
142 contact normal, is related to both the rate of the stress ratio tensor and the plastic strain rate
143 tensor, respectively reflect two different microscopic mechanisms of the fabric evolution. At
144 the initial stage of shearing, as the rapid increase of the stress ratio, contacts are forced to
145 reorganize to support the applied stress. The change of distribution of contact normal, hence
146 the evolution of fabric tensor, is mainly due to the net creation of the contacts, and thus is
147 dominated by the stress ratio rate. This is characterized as the first microscopic mechanisms of
148 the fabric evolution, which is controlled by C_1 and C_2 . At a large shear strain, the net rate of
149 contact creation decreases considerably, and the change of contact normal distribution is
150 controlled by the migration of contact point through sliding and rolling of particles across each
151 other, which can be assumed to be related to the plastic strain rate. This is characterized as the
152 second microscopic mechanisms of the fabric evolution, which is controlled by C_3 .

153 This evolution law captures the fabric evolution law in the entire stress ratio range and all
154 loading directions under a monotonic loading. These findings have been validated with a
155 satisfactory agreement by monotonic DEM simulations. Details of the validation can be found
156 in Hu [42]. However, the effects of b-value have not been fully considered in this evolution
157 law, which will be shown as follows.

158 **2.1 Influence of b-value on the critical stress ratio**

159 From equation (2.2), we see that C_F is dependent on the critical stress ratio and the critical
160 fabric anisotropy. It is well known that the critical stress ratio $M = \eta_c$ is dependent on b-value
161 or Lode angle θ_l . The following equation [28, 33] is used to characterize the relationship
162 between M and Lode angle θ_l :

$$163 \quad M(\theta) = M_{cc} h_1(\theta), h_1(\theta) = \left(\frac{2l_1^4}{1+l_1^4+(1-l_1^4)\sin(3\theta_l)} \right)^{1/4}, l_1 = \frac{M_{ct}}{M_{cc}} \quad (3.1)$$

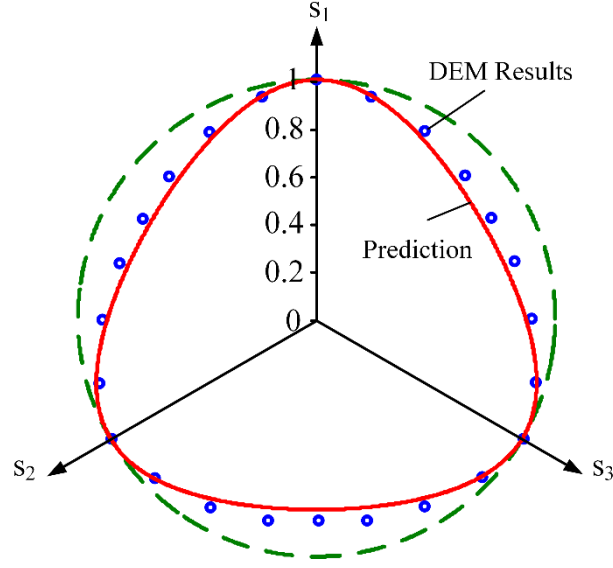
164 where M_{ct} and M_{cc} are the critical stress ratios for triaxial compression and extension. If we
 165 assume that the frictional angles on the shear plane for both extension and compression are the
 166 same, it can be estimated that

$$167 \quad M_{cc} = \frac{6\sin(\phi_{cv})}{3-\sin(\phi_{cv})}, M_{ct} = \frac{6\sin(\phi_{cv})}{3+\sin(\phi_{cv})}, \sin(\phi_{cv}) = \left(\frac{\sigma_1 - \sigma_3}{\sigma_1 + \sigma_3} \right)_c \quad (3.2)$$

168 where ϕ_{cv} is the critical frictional angle. According to relationships in equation (3.2), l_1 can
 169 be expressed in terms of M_{cc} as

$$170 \quad l_1 = \frac{3}{3+M_{cc}} \quad (3.3)$$

171 In equation (3.1), function $h_1(\theta_l)$ determines the shape of M in the π plane (see Fig. 2). For
 172 triaxial compression loading paths, $\theta_l = -\pi/6$, $h_1(\theta_l) = 1$, $M = M_{cc}$; for triaxial extension
 173 loading paths, $\theta_l = \pi/6$, $h_1(\theta) = l_1$, $M = M_{ct}$. This relationship was proven to be realistic
 174 when compared with experimental data. One merit of this shape function is that it is convex
 175 for a larger range of choices of l_1 [43]. We also use equation (3) to predict the critical stress
 176 ratios for various lode angles from the DEM triaxial compression results obtained by Zhao and
 177 Guo [24]. The comparison between predictions obtained by the relationship in equation (3) with
 178 the DEM simulation results is shown in Fig. 2. Note that the results have been normalized by
 179 $M_{cc} = 0.6\sqrt{3/2}$, and that l_1 is obtained by equation (3.3). It can be seen in Fig. 2 that equation
 180 (3) with l_1 estimated by equation (3.3) can capture the critical stress ratio for different b-values
 181 well.



182

183 Fig. 2 Theoretical predictions and DEM results of critical stress ratios in the π plane

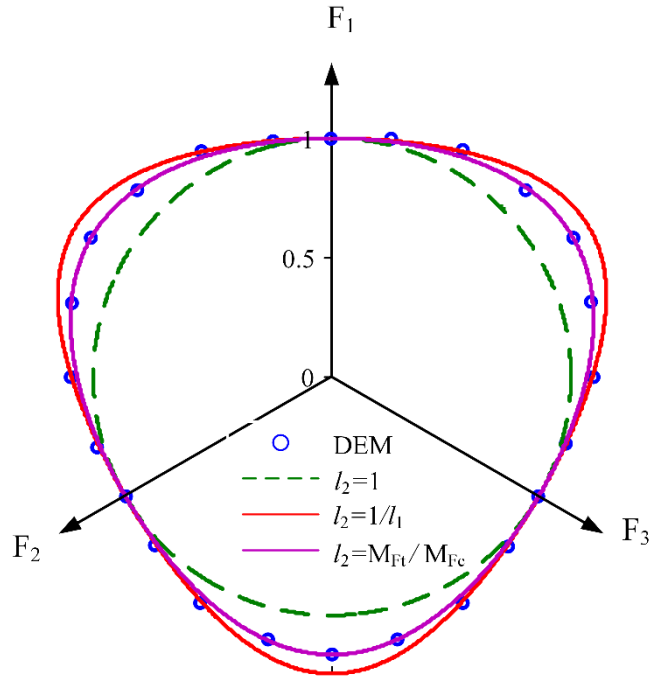
184 **2.2 Influence of b-value on the critical fabric anisotropy**

185 From the DEM tests results [24] in Fig. 3, it can be seen that the shape function for the critical
 186 fabric ratio $M_F = F_{qc}$ is not a circle in the π plane, which means that M_F is also dependent on
 187 the Lode angle. A similar shape function to equation (3.1) is observed. However, M_F under
 188 triaxial extension is greater than that under triaxial compression, which is different from the
 189 case for a critical stress ratio. The differences imply that the shape parameter l_2 for critical
 190 fabric anisotropy should be different from the shape parameter l_1 for the critical stress ratio.
 191 The critical fabric ratio M_F is assumed to be a function of Lode angle as

192
$$M_F(\theta_l) = M_{Fc} h_2(\theta_l), h_2(\theta_l) = \left(\frac{2l_2^4}{1+l_2^4+(1-l_2^4)\sin(3\theta_l)} \right)^{1/4}, l_2 = \frac{M_{Ft}}{M_{Fc}} \quad (4)$$

193 where M_{Ft} and M_{Fc} are the critical fabric ratios for triaxial compression and extension shearing,
 194 respectively. In equation (4), $h_2(-\pi/6) = 1, M_F = M_{Fc}; h_2(\pi/6) = 1, M_F = M_{Ft}$. An
 195 empirical equation based on the DEM test results carried out by Zhao and Guo [24] suggests
 196 that

$$l_2 = 1/l_1 \quad (5)$$



198

199 Fig. 3 Theoretical predictions and DEM results of critical fabric ratios in the deviatoric plane
 200 In general, we can choose l_1 and l_2 independently. If M_{F_t}/M_{F_c} is not available, then we can
 201 use equation (5) to estimate l_2 instead. Fig. 3 presents the comparison between the predictions
 202 from the relationship in equation (4) with different choices of shape parameter l_2 and the DEM
 203 results by Zhao and Guo [24], in which the fabric deviator $M_F(\theta_l)$ has been normalized by M_{F_c} .
 204 It can be seen that the prediction of equation (4) perfectly agrees with the DEM results. The
 205 estimation of l_2 by equation (5) leads to an acceptable gap between the DEM results and the
 206 theoretical prediction.

207 2.3 The generalized fabric evolution law

208 The dependency of $M_F(\theta_l)$ and $M(\theta_l)$ on different shape parameters makes C_F dependent on
 209 the Lode angle. The second term on the right side of the evolution law in equation (2.1)
 210 represents the second evolution mechanism related to the plastic strain rate. The dependency
 211 of C_F on the Lode angle introduces the effect of b-value on the second evolution law

212 mechanism. The first term on the right side of the evolution law in equation (2.1) represents
 213 the first fabric evolution mechanism related to the rate of stress ratio increment and dominates
 214 before reaching the peak stress ratio. To consider the effects of b-value on the first fabric
 215 evolution mechanism, C_1 is assumed to be dependent on the Lode angle and is replaced by
 216 $C_1 h_3(\theta_l)$ with a new shape parameter l_3 . The shape function $h_3(\theta_l)$ is written as

$$217 \quad h_3(\theta) = \left(\frac{2l_3^4}{1+l_3^4+(1-l_3^4)\sin(3\theta_l)} \right)^{1/4}, \quad l_3 = 1/l_1 \quad (6)$$

218 This estimation is proposed based on the observation from the DEM results from Thornton [13,
 219 23]. Thornton presents the response of fabric anisotropy in the π plane for different b-values at
 220 different shearing strain before softening. Compared with the critical fabric anisotropy in Fig.
 221 4, the shape function of the fabric response in the π plane is quite similar at different levels of
 222 the shear strain. The estimation of $l_3 = 1/l_1$ is assumed with the consideration of avoiding too
 223 many material parameters. The consequence of this estimation will be illustrated in details in
 224 section 3.2.

225 A new evolution law considering the effect of b-value is generalized from the hybrid evolution
 226 law in equation (2) as:

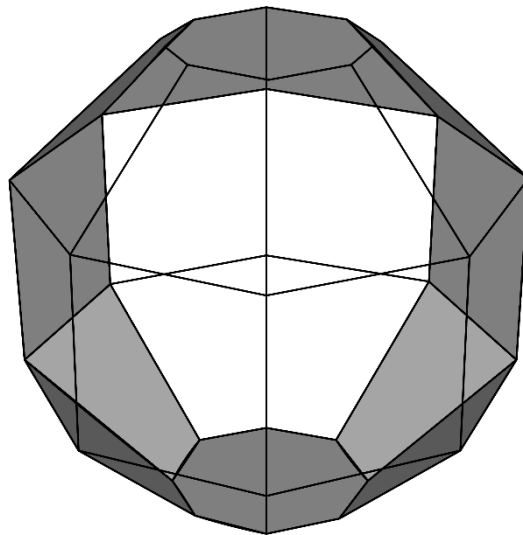
$$227 \quad \dot{\mathbf{F}} = C_1 h_3(\theta_l)(1 + C_2 \|\boldsymbol{\eta}\|)\dot{\boldsymbol{\eta}} + C_3 \dot{\Lambda}(C_F(\theta_l)\boldsymbol{\eta} - \mathbf{F}), \quad C_F(\theta_l) = \frac{M_F(\theta_l)}{M(\theta_l)} \quad (7)$$

228 In this evolution law, the function $C_F(\theta_l)$ considers the effects of b-value on the second
 229 evolution mechanism, while the function $h_3(\theta_l)$ considers the effects of b-value on the first
 230 evolution mechanism. As both function $C_F(\theta_l)$ and $h_3(\theta_l)$ are functions of stress invariants of
 231 the stress tensor, the evolution law satisfies the requirement of the principle of material-frame
 232 indifference. The attractor ' $C_F(\theta_l)\boldsymbol{\eta} - \mathbf{F}$ ' ensures that the new evolution law reaches a unique
 233 critical fabric, which is proportional to the stress ratio tensor $\boldsymbol{\eta}_c$, under monotonic shearing.

234 When we choose the shape parameters as $l_2 = l_1, l_3 = 1$, the evolution law in equation (7)
235 reduces to the evolution law in equation (2).

236 **3 Validation of the generalised evolution law**

237 A series of DEM simulations, by using the PFC^{3D} software ([44]), are performed to validate
238 the generalised evolution law. The behaviour at contacts is modelled by a soft-contact approach,
239 which allows vanishing small overlapping between rigid particles. The linear contact model,
240 i.e., the Hookean model is used to describe the local contact behaviour. **The ratio between the**
241 **tangential and normal stiffness can provide the Poisson's ratio.** In order to minimize possible
242 boundary arching effects, a convex polyhedral (polygonal) shape of the specimen is used, and
243 a set of massless infinite rigid walls are specified to form a polyhedral-shaped boundary (e.g.,
244 Fig.4). The specimen size is chosen to be relatively larger compared with the particle size to
245 accommodate around 11090 and 10151 particles for dense and loose specimens, respectively.



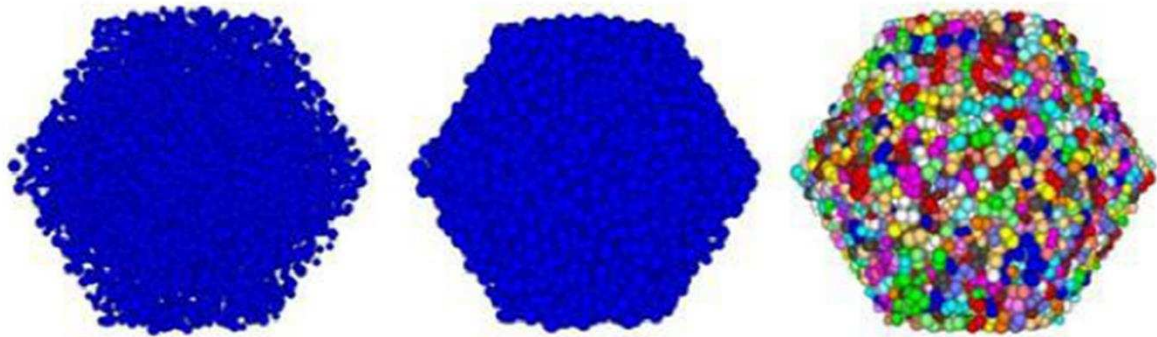
246

247 Fig.4 Example of polyhedron, n=8

248 The main mechanical behaviour of granular materials that we are interested in, e.g., the stress-
249 strain relationship, volumetric strain, shear strain and soil anisotropy, can be reproduced
250 satisfactorily by using spherical particles. The anisotropic packing structure of granular

251 assembly with spherical particles is confirmed by experimental isotropic compression tests
252 (e.g., [45-46]). Hence, the spherical particles are used in this study for the sake of simplicity.

253 A series of parametric studies have been done to determine a proper grain radius range, which
254 can balance the number of particles and the computational efficiency. In addition, a larger range
255 of grain radius may result in the fact that small particles enter into the voids between the larger
256 particles. Hence in this study, the radius of spherical particles consisting of numerical sample
257 is randomly distributed between the range of 0.3mm and 0.5mm.



258 (a) Ball particles with reduced radii

(b) Restored ball radii

(c) Ball replaced by clump

259 Fig. 5 Isotropic sample preparation by the radius expansion method

260 The sample of spherical particles is prepared by using the radius expansion method to generate
261 initial isotropic sample with varying initial void ratios (Fig.5). The dense and loose samples
262 with spherical particles are generated by specifying the frictional coefficients $u_g=0.5$ and $u_g=0.1$,
263 respectively. Then the samples are isotropically consolidated to the confining pressure of
264 $p=500\text{kPa}$. At this stage, the initial void ratios are 0.64 and 0.79, corresponding to dense and
265 loose samples. Then the friction coefficient u is restored to the representative value $u=0.5$ and
266 the samples are ready for simulations. The drained true triaxial loading path is applied, and the
267 principal direction \mathbf{n}^σ is unchanged while the deviatoric strain ε_q continuously increases. A
268 mixed controlled boundary is employed with partially stress-controlled and partially strain-
269 controlled, details can be referred to Li et al [15, 47]. During monotonic shearing for all tests,
270 the mean pressure remains at 500 kPa with various b-values. The b-value ranges from 0 to 1 at

271 an interval of 0.2. Since simulations of quasi-static granular material behaviour are focused,
 272 the mechanical damping is introduced to dissipate energy by damping particle motions. The
 273 local damping is employed. In the virtual experiments to be presented, the Cauchy stress and
 274 Biot strain definitions are followed [48]. The input parameters for the DEM simulation are
 275 listed in Table 1.

276 Table 1 DEM simulation properties

Number of particles	Dense specimen: 11090 Loose specimen: 10151
Particle solid density ρ	2700 kg/m ³
Spherical particle radius r	[0.3,0.5] mm
Contact model	Linear stiffness
Normal stiffness for ball and wall	$k_n=1 \times 10^5$ N/m
Tangential stiffness for ball and wall	$k_s=1 \times 10^5$ N/m
Initial void ratio e_0	Dense specimen: 0.64 Loose specimen: 0.79
Target loading path	True triaxial
Damping coefficient	$x=0.7$

277

278 The implicit Euler algorithm is used to integrate the evolution law. The evolution law in a rate
 279 form can be rewritten as

$$280 \quad \mathbf{F}_{n+1} - \mathbf{F}_n = C_1 h_3(\theta_{n+1})(1 + C_2 \|\boldsymbol{\eta}_{n+1}\|)(\boldsymbol{\eta}_{n+1} - \boldsymbol{\eta}_n) + C_3 \dot{\Lambda}(C_F(\theta_{n+1})\boldsymbol{\eta}_{n+1} - \mathbf{F}_{n+1}) \quad (8.1)$$

281 where $\dot{\Lambda}$ is a discrete form of the norm of deviatoric plastic strain rate, i.e.

$$282 \quad \dot{\Lambda} = \|\mathbf{e}_{n+1} - \mathbf{e}_n\| \quad (8.2)$$

283 We arrive at a sub load step n+1, as:

$$284 \quad \mathbf{F}_{n+1} = \frac{C_1 h_3(\theta_{n+1})(1 + C_2 \|\boldsymbol{\eta}_{n+1}\|)(\boldsymbol{\eta}_{n+1} - \boldsymbol{\eta}_n) + \dot{\Lambda} C_3 C_F(\theta_{n+1})\boldsymbol{\eta}_{n+1} + \mathbf{F}_n}{1 + C_3 \dot{\Lambda}} \quad (8.3)$$

285 Then, given that the initial fabric tensor $\mathbf{F}_1 = \mathbf{F}_i$, stress ratios $\boldsymbol{\eta}_{n+1}, \boldsymbol{\eta}_n$ and deviatoric strains
286 $\mathbf{e}_{n+1}, \mathbf{e}_n$, we adopt these stresses and strain paths obtained by DEM tests as the integration
287 paths and calculate the fabric tensor using equation (8.2) for each sub-load step. The parameters
288 used for theoretical predictions are listed in Table 2. The parameters M_{cc}, M_{Fc}, M_{Ft} can be
289 obtained directly from the DEM simulation results directly. From these independent parameters,
290 shape parameters can be obtained. From equation (3), $M_{ct} = 0.62; l_1 = 0.795$. The shape
291 parameter l_2 is determined by the definition of $l_2 = M_{Ft}/M_{Fc}$. The shape parameter l_3 is
292 estimated from equation (6). Parameters C_1, C_2, C_3 , which control the rate of fabric tensor,
293 cannot be determined directly. They are determined by the regressive analysis through the
294 known stress, strain rate and fabric information obtained from DEM simulations. The effects
295 of C_1, C_2, C_3 will be investigated through parametric analysis in section 3.2.

296 Table 2 Parameters of the generalised fabric evolution law

C_1	C_2	C_3	M_{cc}	M_{Fc}	M_{Ft}
0.1	6	7.6	0.78	0.66	0.77

297

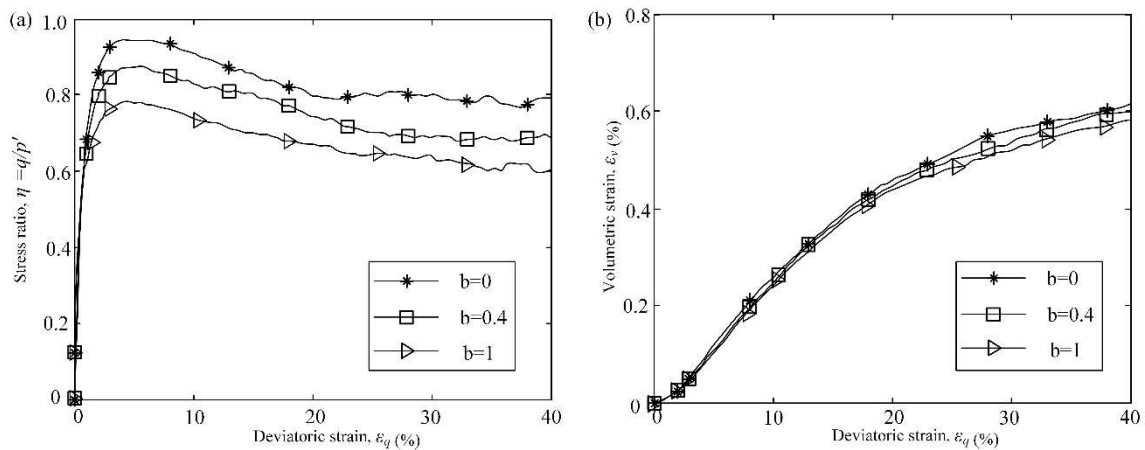
298 3.1 Comparison with DEM simulation results

299 3.11 Comparison of the stress-strain and volumetric strain curve between DEM and 300 experimental results

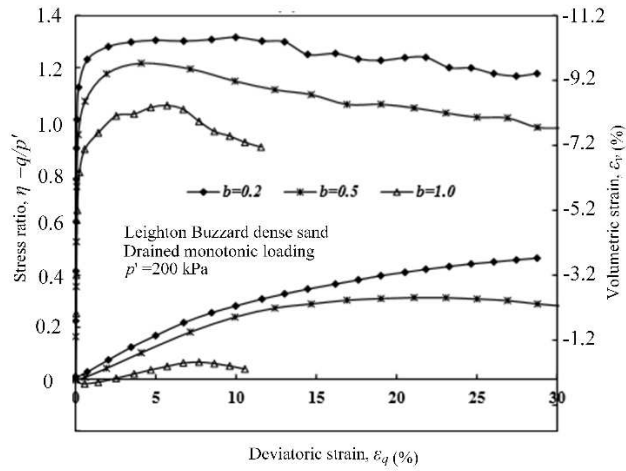
301 Fig.6 and Fig.7 illustrate the effects of b-value on the responses of stress-strain relationships
302 and volumetric strain, respectively obtained from DEM simulations and experimental Hollow
303 Cylinder Testing from Yang et al [12]. Here the dense specimen is taken as an example. It
304 should be noted that Leighton Buzzard sand has been used by Yang et al [12], which is different
305 from the samples that are used in our study. Hence, we only focus on the comparison of the
306 trend other than the exact magnitude, between the DEM simulation results and experimental

307 results. Regarding the effects of b-value on the stress strain curves as shown in Fig. 6 (a) and
 308 Fig.7, the trends of both curves obtained from the DEM simulations and laboratory testing,
 309 respectively are consistent. The stress ratio is decreasing with an increase in the b-value.
 310 Volumetric strains start to dilate at the beginning of shearing, and more dilative behaviour are
 311 observed at a greater b-value, for both DEM simulations and experimental findings (Fig.6 b
 312 and Fig.7). The only difference is that the variation of dilatancy is larger showing by the
 313 experimental results, when compared to the DEM simulation results. This difference may be
 314 attributed to the fact that shear band develops quickly for the hollow cylindrical sample;
 315 however, shear band is not considered in our DEM simulations.

316 Similar experimental investigations regarding effects of b-value on sand behaviours, in terms
 317 of the stress-strain and volumetric strain, have been reported for dense samples in the literature
 318 (e.g., [6, 49]). The investigations regarding the loose samples can be referred to Li et al [15]
 319 and Yang et al [12].



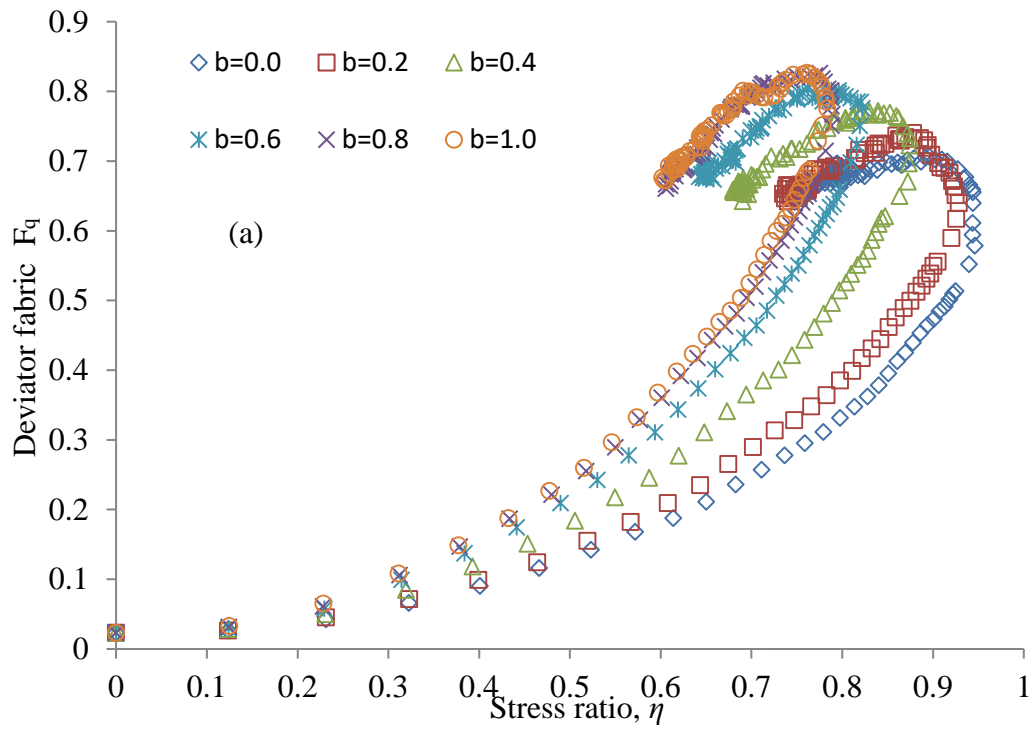
320
 321 Fig.6 DEM simulation results on the effects of b-value on the response of stress-strain
 322 relations and volume change behaviours



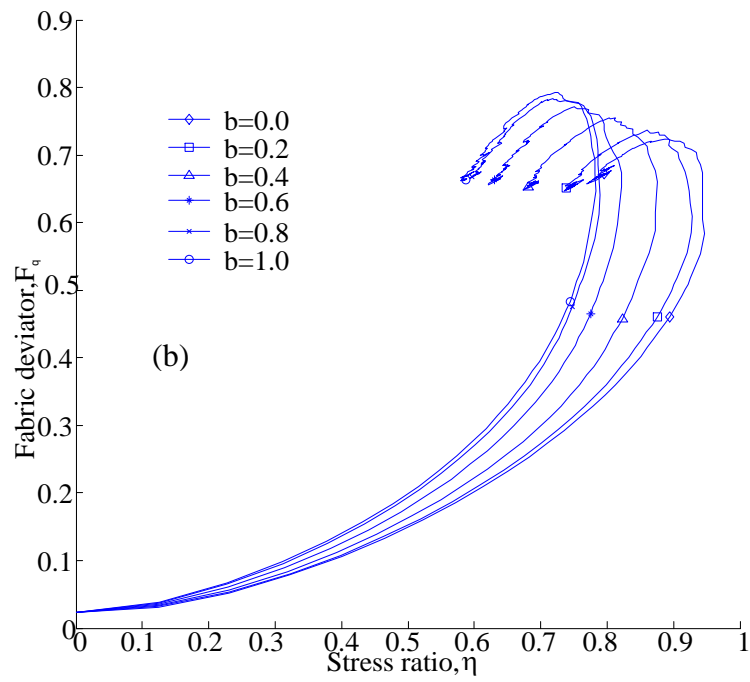
323
 324 Fig.7 Hollow Cylinder experimental results on the effects of b-value on the response of
 325 stress-strain relations and volume change behaviours ([12])

326 3.12 Evolution of fabric deviator against the stress ratio

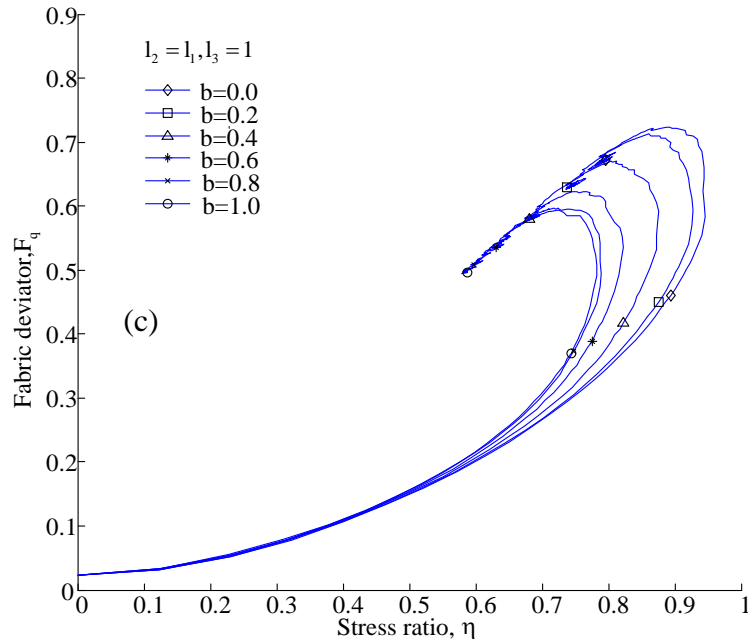
327 Fig.8 presents the evolution of the fabric deviator against the stress ratio for both DEM
 328 simulation results and theoretical results predicted by equation (2) and equation (7), in terms
 329 of dense specimens. Note that equation (2) is recovered from equation (7) by designating that
 330 $l_2 = l_1, l_3 = 1$. It can be clearly seen from the DEM results that the evolution of the fabric
 331 deviator for different b-values follows a similar pattern. The fabric deviator increases with the
 332 stress ratio at the initial stage of shearing until the stress ratio peaks. After that, the fabric
 333 deviator also achieves the peak value with a slight lag. The fabric deviator begins to decrease
 334 as the decreasing stress ratio continues to reach the critical value.



335



336



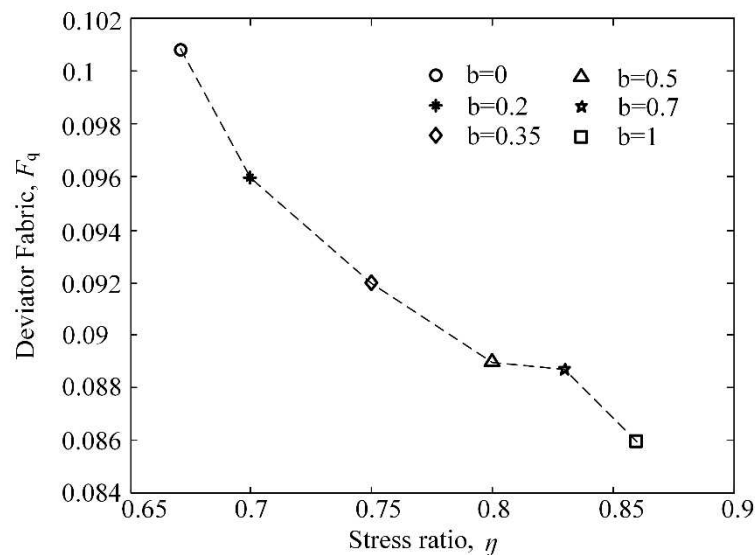
337

338 Fig. 8 The fabric evolution under proportional loading (dense sample): stress ratio η vs fabric
 339 deviator Fq : a) DEM simulation results; b) theoretical results from equation (7); c) theoretical
 340 results from equation (2).

341 The micromechanical interpretation of this phenomenon can be given through the stress-force-
 342 fabric (SSF) relationship proposed by Quadfel and Rothenburg [21]. In their study, the stress
 343 ratio was linearly related to the anisotropy degrees for contact normal density (i.e., fabric
 344 deviator) and the rest (e.g., normal contact force, tangential contact force, particle shape). The
 345 fabric deviator would follow the stress ratio to increase to a peak value. However, the
 346 anisotropy degrees for the rest would as well contribute to the stress ratio. According to the
 347 fabric evolution mechanism, the fabric deviator would exhibit a slag before approaching the
 348 peak value, and then decreased with the decreasing of the stress ratio to achieve a critical state.
 349 Yang [50] has analysed the evolution of contact normal by the DEM simulation results to
 350 explain this phenomenon. He presented that the vertical contact orientation is getting narrower,
 351 while the horizontal orientation is getting wider, with the increasing of shearing. The deviatoric
 352 stress ratio was increased since the sample was compressed. At the initial stage, the distribution
 353 of contact normal was homogeneous, demonstrating an isotropic state. The contact normal was
 354 continuously oriented to the vertical direction with the increasing of shearing. The fabric

355 deviator was increasing until approaching a peak value. After that, the distribution of contact
 356 normal in the vertical direction was generally decreasing until reaching a critical state.

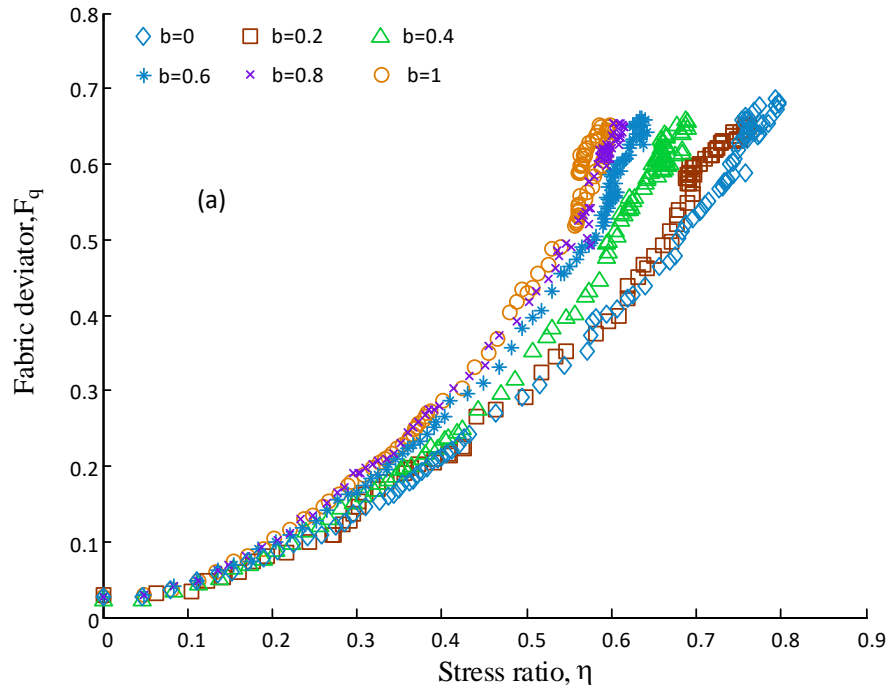
357 The b -value affects the peak and critical values of the fabric deviator; meanwhile, it affects the
 358 change of fabric deviator against the stress ratio. The peak fabric deviator increases with a
 359 greater b -value, while the peak stress ratio decreases with an increasing b -value, which is
 360 consistent with the observations by Thornton and Zhang [23] (Fig. 9). The evolution law in
 361 equation (7) can quantitatively capture the evolution of the fabric deviator.



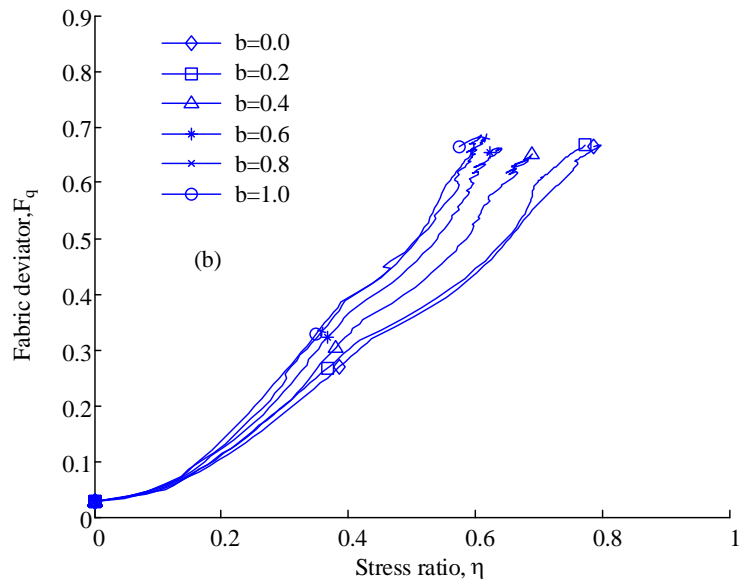
362 Fig.9 The peak stress ratio η vs fabric deviator Fq (Thornton and Zhang, 2010)

363
 364
 365 Fig.10 presents the evolution of the fabric deviator against the stress ratio for both DEM
 366 simulation results and theoretical results predicted by equation (7), in terms of loose specimens.
 367 Likewise, the evolution of the fabric deviator for different b -values follows a similar pattern.
 368 The fabric deviator increases with an increase in the stress ratio. The theoretical predictions
 369 shown in Fig. 10b can well capture the fabric deviator for a loose specimen. It should be noted
 370 that the present fabric evolution law is proposed by characterizing the influence of b -value on
 371 the critical state stress and critical state fabric; however, the critical state is not dependent on
 372 the initial void ratios (Yang [50]). Hence, comparisons between the DEM simulation results

373 and theoretical predictions for both dense and loose samples demonstrate the applicability of
 374 the proposed evolution law to cases with various initial void ratios.



375



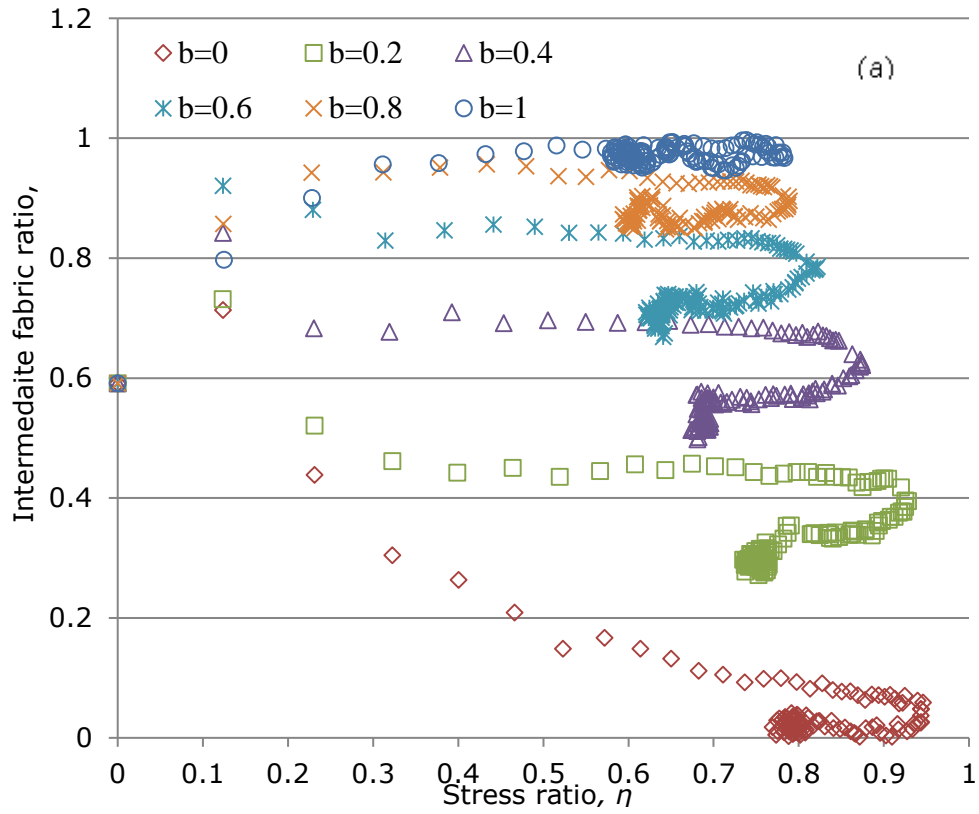
376

377 Fig.10 The fabric evolution under proportional loading (loose sample): stress ratio η vs fabric
 378 deviator F_q : a) DEM simulation results; b) theoretical results from equation (7)

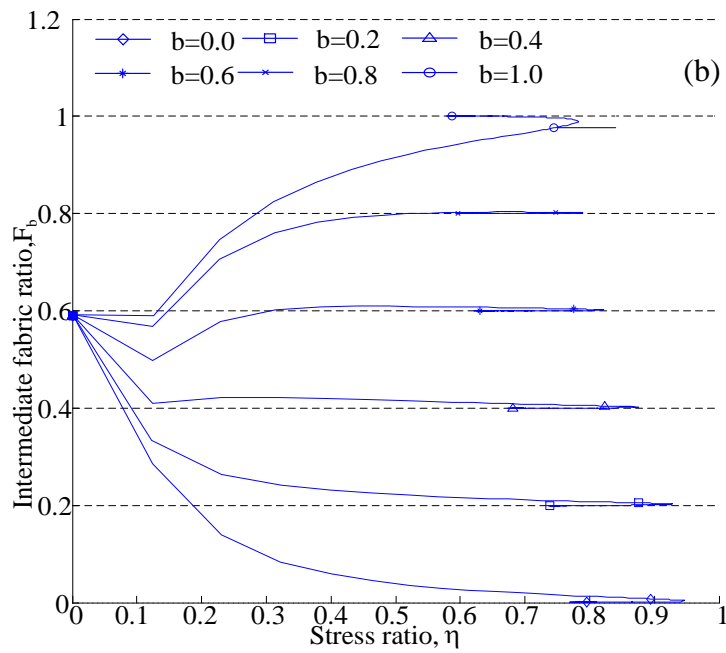
379

380 3.13 Evolution of the intermediate fabric ratio against the stress ratio

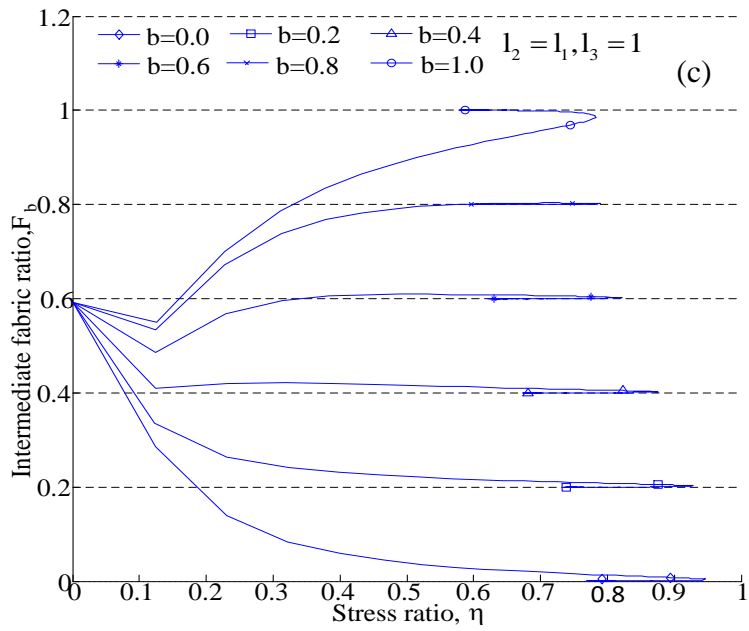
381 Fig. 11 and Fig.12 present the evolution of the intermediate fabric ratio F_b ($F_b =$
382 $(F_2 - F_3)/(F_1 - F_3)$) against the stress ratio for both DEM simulated results and theoretical
383 predictions, corresponding to the dense and loose specimens, respectively. It can be seen from
384 Fig. 11 and Fig. 12 that the evolution law in equation (7) can generally capture the effect of b-
385 value on the evolution of F_b . For the dense specimen as shown in Fig. 11, in theoretical
386 prediction, F_b reaches the b-value quickly before the peak stress ratio. In DEM results, even
387 after the peak stress ratio, F_b still evolves towards the value of the intermediated stress ratio.
388 In the fabric evolution law, it is assumed that the fabric tensor evolves towards the critical state
389 and at the critical state F_b is the same as the b-value. With respect to the loose specimen as
390 shown in Fig.12 a, F_b evolves towards the value of the intermediate stress ratio without a peak
391 value. The theoretical predictions show that the fabric tensor evolves towards the critical state,
392 where a larger final stress ratio is reached with a lower b-value. However as shown in both Fig.
393 11a and Fig. 12a, in DEM results, the final F_b is not exactly as the b-value, even it evolves
394 towards b-value. This is because **the real critical state is difficult to be achieved in DEM**
395 **simulations due to the use of spheres in this study**. The shear strain is not fully developed to
396 give a critical state, since the shear strain is loaded to 40% in this study and the polyhedral
397 shape used in our study can satisfactorily guarantee homogeneity of the sample [51]. Many
398 researchers (e.g., [52]) have pointed out that critical states can only be reached at very large
399 local shear deformations, e.g., the shear strain develops 70% or 100%, which are not always
400 obtained by biaxial compression tests (both physical and numerical). **Things would be different**
401 **if non-spherical grains are used, which will be analysed in the future work.**



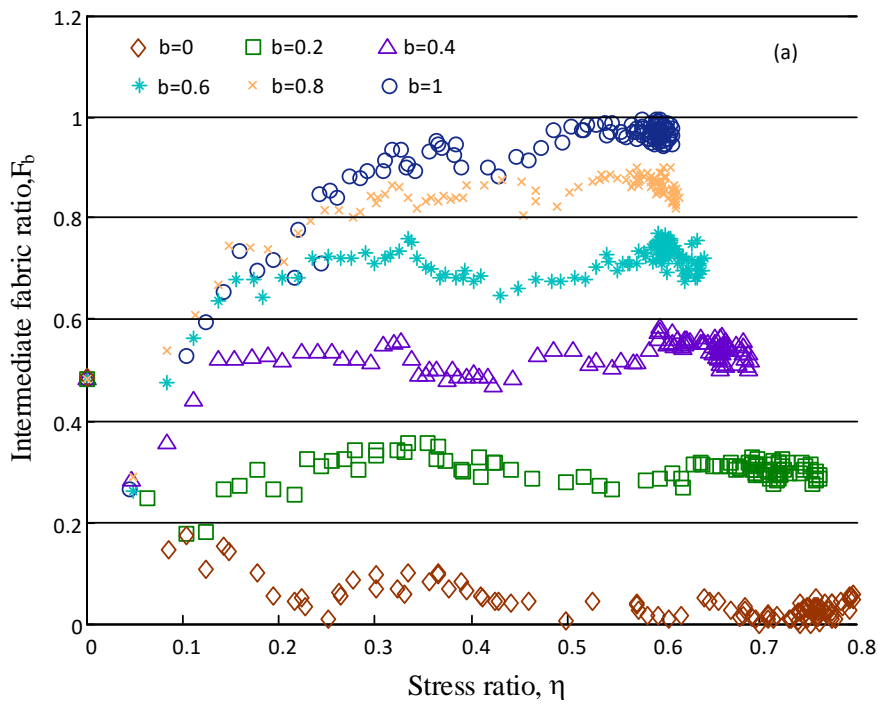
402

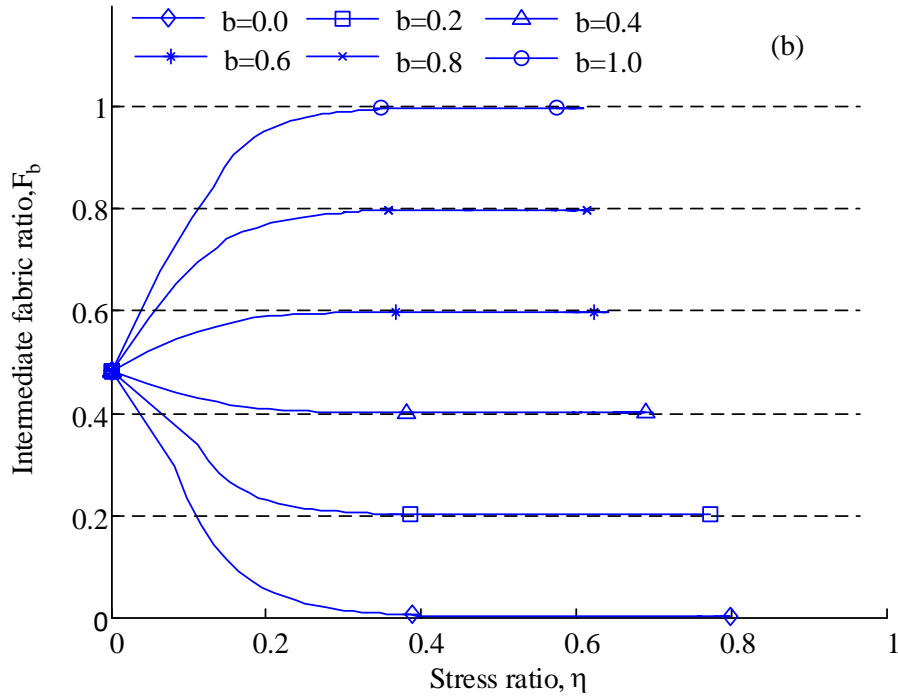


403



405 Fig. 11 The fabric evolution under proportional loading (dense sample): the stress ratio η vs
 406 the intermediate fabric ratio F_b : a) DEM simulation results; b) theoretical results from
 407 equation (7); c) theoretical results from equation (2).





410

411 Fig. 12 The fabric evolution under proportional loading (loose sample): the stress ratio η vs
 412 the intermediate fabric ratio F_b : a) DEM simulation results; b) theoretical results from
 413 equation (7).

414 There is a large difference between the prediction and DEM results at a low stress ratio. This
 415 may be because the initial fabric of the sample used in DEM simulations is almost isotropic,
 416 i.e., the fabric deviator is very small. Hence the F_b is approximately singular. From this point
 417 of view, the DEM simulation results for F_b are meaningless at very small stress ratios because
 418 they cannot be accurately measured. The gap between the theoretical predictions and DEM
 419 simulation results, may be caused by the fact that the newly proposed evolution law is only
 420 concerned with two main mechanisms of the fabric evolution, i.e., the net rate of contact
 421 creation and migration of contact point, at a particle scale as shown in equation (7). Other
 422 secondary fabric evolution mechanisms, e.g., the convection and diffusion processes of
 423 contacts (due to that the contacts are continually created and broken during the deviatoric
 424 loading after the mitigation of contact points), are not taken into consideration. These
 425 secondary fabric mechanisms have been demonstrated not to be the main concern (e.g., [17,
 426 51]).

427

428 Theoretical predictions by the evolution law in equation (2) are also presented in Fig.8c and
429 Fig. 11c. In equation (2), C_F is taken as a constant independent of b-value. In a theoretical
430 prediction, the integration stress-strain path is the true stress-strain path taken from DEM
431 simulation results, and the critical stress ratio decreases with an increasing b-value. From
432 equation (2.2), we can deduce that the predicted critical fabric anisotropy, determined by $M_F =$
433 $C_F M$, also shows a similar trend as shown in Fig.8c. However, DEM results do not exhibit a
434 similar trend. The predicted peak fabric anisotropy decreases with the increase in the b-value,
435 which is obviously contradictory to the DEM results. The independency of C_F and C_1 from the
436 b-value does not affect the predictions of F_b mainly because the initial fabric is almost isotropic
437 and the increment of fabric tensor is proportional to the deviatoric stress tensor; hence, F_b
438 approaches the intermediate stress ratio quickly in both predictions by both equations (2) and
439 (7). When the initial fabric tensor is highly anisotropic, the approach of F_b to the intermediate
440 stress ratio will be slower, and the performance of the fabric evolution law should be better,
441 which can be shown by the results of the evolution of F_b in Hu [42].

442 From these comparisons, the generalized evolution law in equation (7) captures the effects of
443 b-value on the fabric evolution well and greatly improves the performance of the evolution law
444 in equation (2) in terms of the fabric deviator.

445

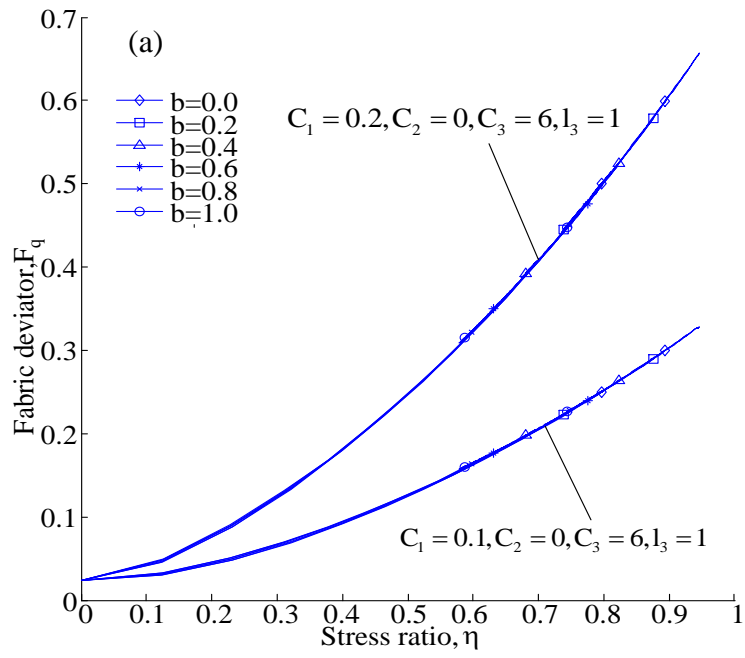
446 **3.2 Parametric analysis**

447 In the following computations, the shape parameters l_1 and l_2 are assumed to be the same as
448 those used in the section 3.1. In all cases, the intermediate fabric ratio F_b and the principal
449 directions of the fabric tensor quickly approach the stress tensor; hence, in the following
450 analysis, only the results of the fabric deviator are presented in terms of the dense sample. The

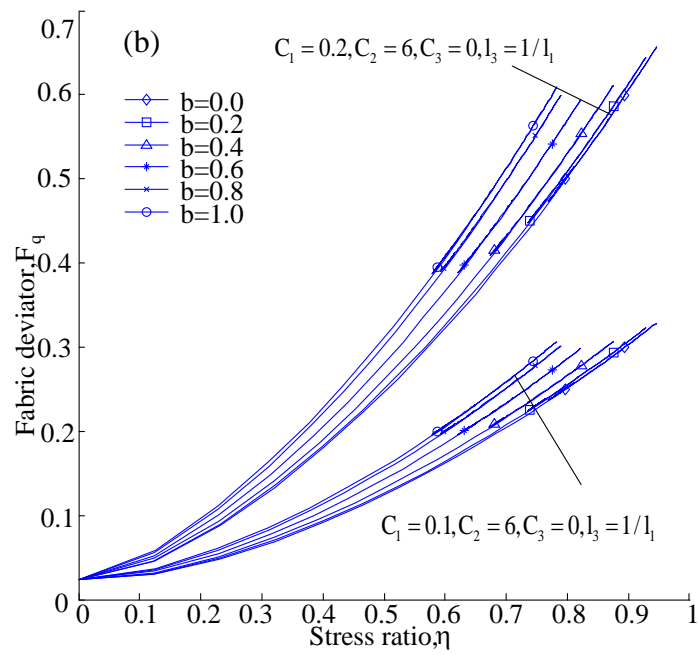
451 dense sample is taken as an example for simplicity since the following parameters are not
452 obviously affected by the initial void ratio.

453 3.2.1 Parameter C_1 and shape parameter l_3

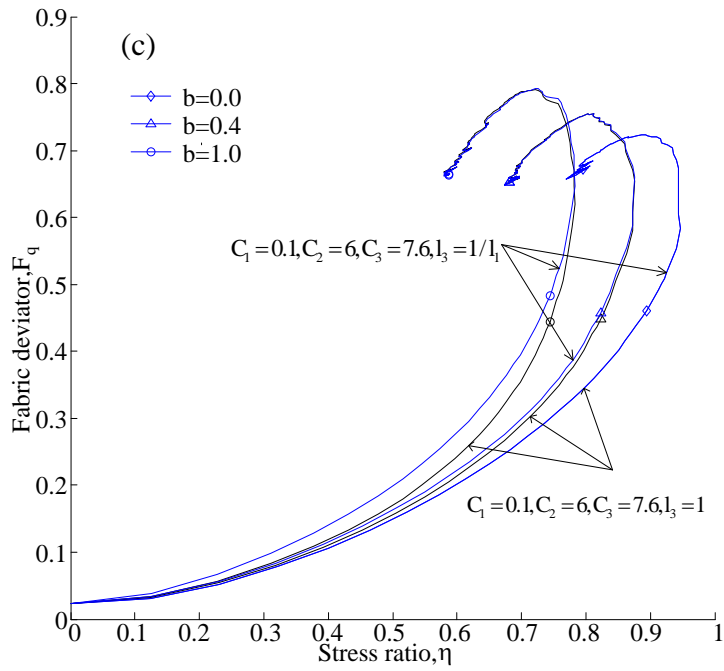
454 By comparing Fig. 13a with Fig. 13b, the effects of shape parameters l_3 on the first evolution
455 mechanism related to the stress ratio tensor can be seen. As noted before, the first fabric
456 evolution mechanism dominates the fabric evolution at a low stress ratio, because the plastic
457 strain is negligible at this stage. When $l_3 = 1$, the shape function h_3 becomes independent of
458 the b-value, and the predicted fabric deviators for different b-values coincide for the same C_1 .
459 However, when $l_3 = 1/l_1 > 1$, the shape function h_3 is an increasing function with a greater
460 b-value, and fabric deviators increase quicker for a larger b-value. From both Fig. 13a and Fig.
461 13b, we can see that the rate of the fabric deviator increases with increasing C_1 . Fig. 13c and
462 Fig. 13d present the effects of the parameter C_1 and shape parameter l_3 on the evolution law.
463 From Fig. 13c, we can see that because the second fabric evolution mechanism is also involved,
464 the influence of l_3 on the fabric evolution decays with an increase in the stress ratio; after the
465 peak stress ratio, the effects almost totally disappear. It can be seen in Fig. 13c that C_1 has a
466 strong effect on the evolution of F_q up to the peak fabric deviator. However, after the peak
467 stress ratio, the influence disappears gradually until the critical stress ratio. Because parameters
468 C_1 and l_3 affect the fabric evolution through the first mechanism, their influences disappear
469 when the influence of the first mechanism diminishes after the peak stress ratio.



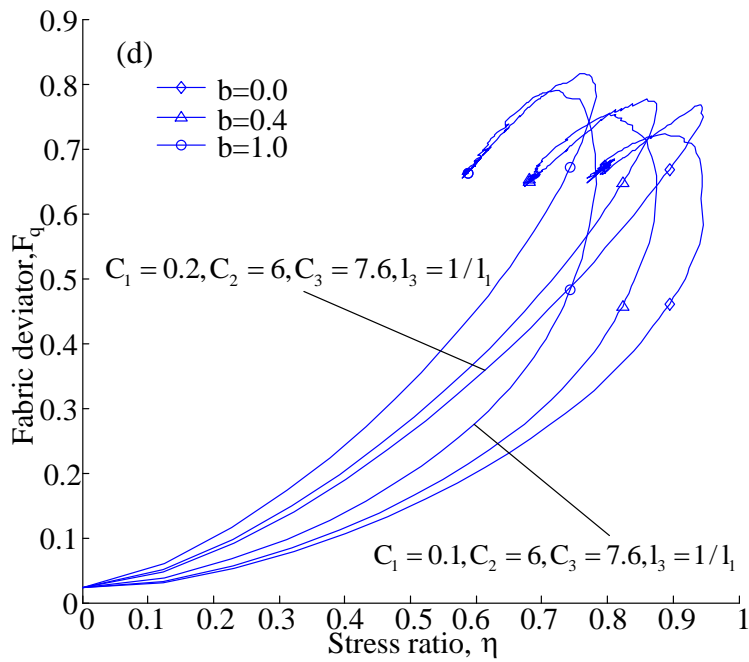
470



471



472



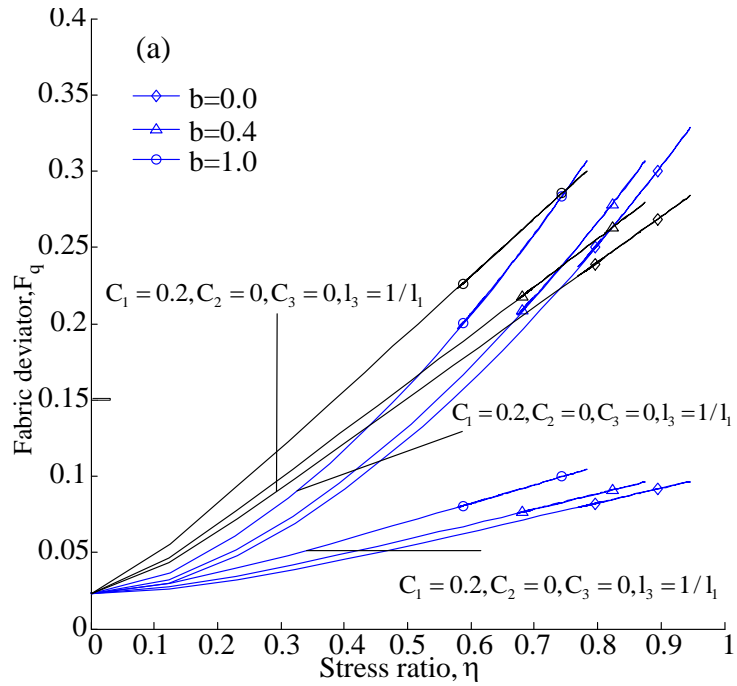
473

474 Fig. 13 Influences of C_1 and l_2 on the fabric deviator evolution

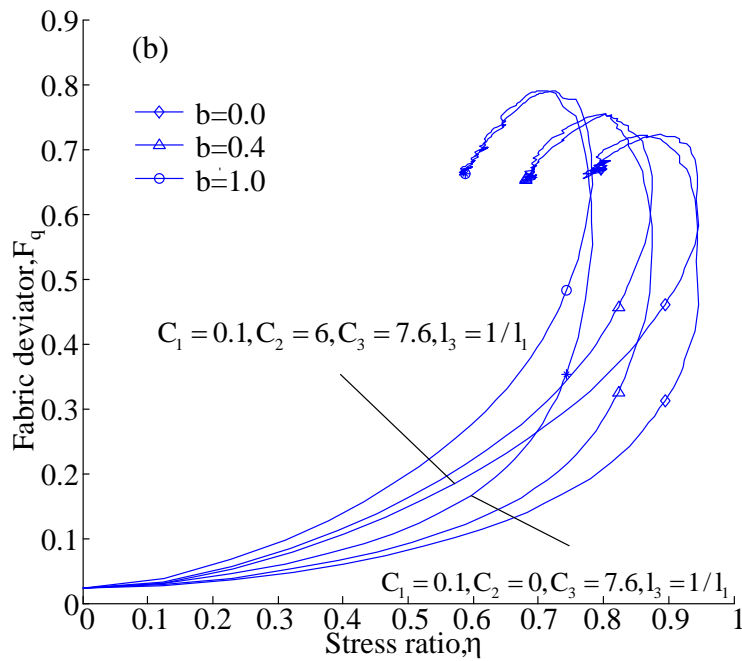
475 3.2.2 Parameter C_2

476 Parameter C_2 also affects the fabric evolution through the first evolution mechanism. In Fig.
 477 14a, when the second mechanism is not involved, we can see that C_2 mainly affects the rate of
 478 increase of the fabric deviatoric against the stress ratio. When $C_2 = 0$, the relationship between

479 Fq and η becomes approximately linear. When $C_2 \neq 0$, the relationship is approximately
 480 quadric. For some case when simplicity is the primary concern rather than the accuracy, we
 481 can simply set $C_2 = 0$ together with another choice of C_1 to replace a more accurate set of C_1
 482 and C_2 . Fig. 14b again shows that the effects of C_2 last until the peak stress ratio, after which
 483 the effect of C_2 disappears.



484



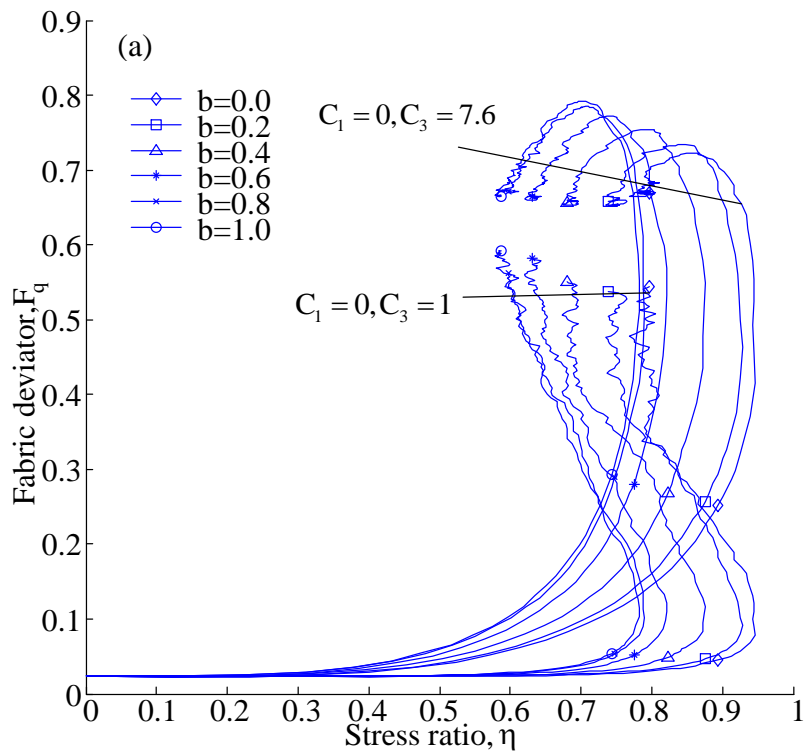
485

486

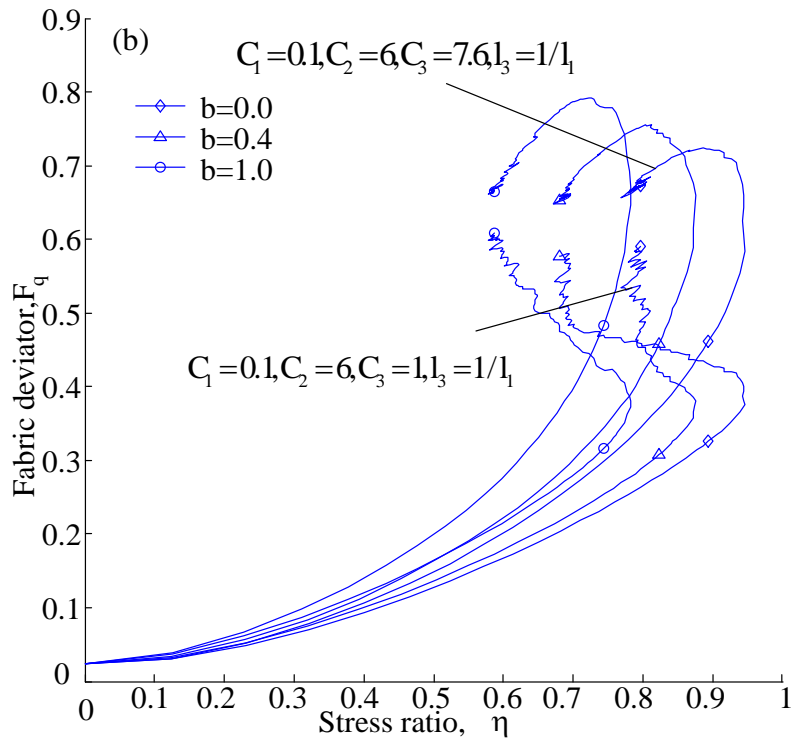
Fig. 14 Influences of C_2 on the fabric deviator evolution

487 3.2.3 Parameter C_3

488 Parameter C_3 affects the fabric evolution through the second evolution mechanism related to
489 the plastic stress rate. The second mechanism ensures that the fabric evolves towards the critical
490 fabric. In Fig.15 a, when the first mechanism is not involved, we can see that C_3 increases the



491



492

493

Fig. 15 Influences of C_3 on the fabric deviator evolution

494

rate of the fabric deviator towards the critical fabric deviator. When C_3 is smaller, the fabric

495

evolves slower. C_3 does not have obvious effects on the fabric evolution at a low stress ratio;

496

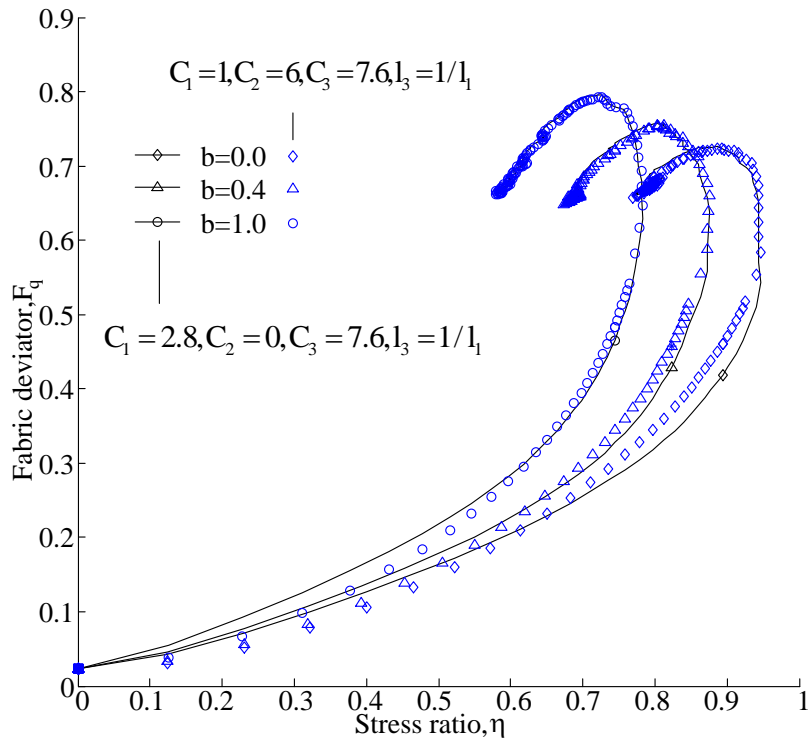
the influence of C_3 increases with an increasing stress ratio. If C_3 is not large enough, the

497

evolution law may not predict a peak fabric deviator. When the first evolution mechanism is

498

involved, as shown in Fig. 15 b, similar effects of C_3 on the fabric evolution can be observed.



499

500 Fig. 16 Influences of the assumption $C_2 = 0, l_3 = 1/l_1$ on fabric deviator evolution

501 3.2.4 Discussion

502 From the parametric analysis, parameters C_1, C_2, l_3 affect the fabric evolution from the first
503 mechanism, which dominates the fabric evolution at a low stress ratio. Parameter C_3 affects the
504 fabric evolution from the second mechanism, which dominates the fabric evolution after the
505 peak stress ratio when considerable plastic strain occurs. From this feature, we can determine
506 the parameter C_3 by fitting curves of the stress ratio vs the fabric deviator after the peak stress
507 ratio for a specific b-value, e.g., triaxial compression, and determine the parameters C_1, C_2, l_3
508 by fitting the curves of the stress ratio fabric deviator at a low stress ratio for a specific b-value.
509 Because the influences of C_2, l_3 decay quickly due to the existence of the second evolution
510 mechanism, we can simply assume that $C_2 = 0, l_3 = 1/l_1$ if the data are not available. Under
511 this assumption, only parameter C_1 is left for determination. When the fabric evolution law is
512 used for constitutive modelling considering the effects of initial and induced anisotropy and b-
513 value, the assumption $C_2 = 0, l_3 = 1/l_1$ can reduce the amount of material parameters. Fig.16

514 presents the fabric deviator against the stress ratio for this assumption. From Fig.16, we can
515 see that this assumption only affects the predicted accuracy at a very low stress ratio.

516 **4 Concluding remarks**

517 In this paper, the effects of b-value on the contact normal-based fabric evolution of granular
518 materials were incorporated into an extant hybrid fabric evolution law. This new fabric
519 evolution had the feature of material-frame indifference, rate-independency and uniqueness of
520 critical state. The new fabric evolution law was validated by DEM simulation results with
521 various initial void ratios. Conclusions can be drawn as follows:

- 522 • The new fabric evolution can capture the effects of b-value on the fabric evolution well
523 for various initial void ratios, especially for the evolution of fabric deviator F_q . There
524 was a gap between the theoretical predictions and DEM simulation results for F_b , due
525 to the fact that only two main mechanisms, i.e., the net rate of contact creation and
526 migration of contact point, of the fabric evolution were concerned in the present fabric
527 evolution law.
- 528 • Parametric study was carried out to analyse the influences of parameters C_1, C_2, C_3, l_3 .
529 For simplicity, the setting of parameters for the fabric evolution law in equation (7) can
530 be reduced to 5 independent parameters, i.e., $(C_1, C_3, M, M_{Fc}, M_{Ft})$.
- 531 • The proposed evolution law can act as a fundamental aid for further development of
532 fabric constitutive modelling of granular materials, accounting for the effects of b-value
533 and material anisotropy, combined with simple isotropic constitutive models (e.g., the
534 CASM Model).

535 In this paper, we limited the stress path in the monotonic loading with a fixed loading direction.
536 The evolution law has not been validated to consider the b-value on fabric evolution for more
537 complicated stress path, e.g., pure rotational shearing, which needs further investigation.

538 **5 Acknowledgement**

539 This work was supported by the National Natural Science Foundation of China (Grant
540 No.51609204, 51608454) and the Fundamental Research Funds for the Central Universities
541 (Grant No. 2682015CX092, 2682016CX084). In addition, the authors would like to thank Prof.
542 Xia Li, School of Civil Engineering in Southeast University, for her valuable guidance and
543 support to this work.

544 **References**

- 545 [1] Habib P. Influence de la variation de la contrainte principale moyenne sur la résistance au
546 cisaillement des sols. Proceedings of the 3rd International Conference on Soil Mechanics and
547 Foundation Engineering 1953;131-136.
- 548 [2] Bishop AW. The Strength of Soils as Engineering Materials. *Géotechnique* 1966;16(2):91-
549 130.
- 550 [3] Bjerrum L, Kummeneje O. Shearing resistance of sand samples with circular and
551 rectangular cross sections. NGI Report, NR 1961;44(1-7).
- 552 [4] Cornforth DH. Some experiments on the influence of strain conditions on the strength of
553 sand. *Géotechnique* 1964;14(2):143-167.
- 554 [5] Oda M, Koishikawa I, Higuchi T. Experimental study of anisotropic shear strength of sand
555 by plane strain test. *Soils and foundations* 1978;18(1):25-38.
- 556 [6] Lade PV, Duncan J M. Cubical Triaxial Tests on Cohesionless Soil. *Journal of the Soil
557 Mechanics and Foundations Division* 1973;99(10):793-812.
- 558 [7] Arthur JRF, Chua KS, Dunstan T. Induced anisotropy in a sand. *Géotechnique*
559 1977;27(1):13-30.
- 560 [8] Nabil, SE. Shear strength of a cohesionless soil under plane strain and triaxial conditions. ,
561 Open Access Dissertations and Theses. Paper 484; 1976.
- 562 [9] Symes MJ. Rotation of principal stresses in sand. PhD Thesis, Imperial College of Science,
563 Technology and Medicine, University of London, 1983.
- 564 [10] Sayao ASFJ, Vaid YP. Effect of intermediate principal stress on the deformation response
565 of sand. *Canadian Geotechnical Journal* 1996;33(5):822-828.

- 566 [11] Yoshimine M, Ishihara K, Vargas W. Effects of principal stress direction and intermediate
567 principal stress on undrained shear behavior of sand. *Soils and Foundations* 1998;38(3):179-
568 188.
- 569 [12] Yang, L.T. Li, X. Yu, H.S. Wanatowski, D. A laboratory study of anisotropic geomaterials
570 incorporating recent micromechanical understanding, *Acta Geotechnica* 2016; 11:1111.
- 571 [13] Thornton C. Numerical simulations of deviatoric shear deformation of granular media.
572 *Géotechnique* 2000;50(1):43-53.
- 573 [14] Thornton C, Zhang L. A numerical examination of shear banding and simple shear non-
574 coaxial flow rules. *Philosophical Magazine* 2006;86(21-22):3425-3452.
- 575 [15] Li X., Yang D.S., Yu. H-S. Macro deformation and micro structure of 3D granular
576 assemblies subjected to rotation of principal stress axes, *Granular Matter* 2016, 18:53.
- 577 [16] Li B, Chen LL, Gutierrez M. Influence of the intermediate principal stress and principal
578 stress direction on the mechanical behavior of cohesionless soils using the discrete element
579 method. *Computers and Geotechnics* 2017;86:52-66.
- 580 [17] Kuhn MR. Micro-mechanics of fabric and failure in granular materials. *Mechanics of*
581 *Materials* 2010;42(9):827-840.
- 582 [18] O'sullivan C, Wadee MA, Hanley KJ, Barreto D. Use of DEM and elastic stability analysis
583 to explain the influence of the intermediate principal stress on shear strength. *Géotechnique*
584 2013;63(15):1298-1309.
- 585 [19] Kanatani KI. Distribution of directional data and fabric tensors. *International Journal of*
586 *Engineering Science* 1984;22(2):149-164.
- 587 [20] Li X, Yu HS, Li XS. Macro–micro relations in granular mechanics. *International Journal*
588 *of Solids and Structures* 2009;46(25):4331-4341.
- 589 [21] Ouadfel H, Rothenburg L. 'Stress–force–fabric' relationship for assemblies of ellipsoids.
590 *Mechanics of materials* 2001;33(4):201-221.
- 591 [22] Li X, Yu HS. On the stress–force–fabric relationship for granular materials. *International*
592 *Journal of Solids and Structures* 2013;50(9):1285-1302.
- 593 [23] Thornton C, Zhang L. On the evolution of stress and microstructure during general 3D
594 deviatoric straining of granular media. *Géotechnique* 2010;60(5):333-341.
- 595 [24] Zhao J, Guo N. Unique critical state characteristics in granular media considering fabric
596 anisotropy. *Géotechnique* 2013a;63(8):695-704.
- 597 [25] Matsuoka H, Nakai T. Stress-deformation and strength characteristics of soil under three
598 different principal stresses. *Proceedings of the Japan Society of Civil Engineers: Japan Society*
599 *of Civil Engineers*, 1974. 232:59-70.

- 600 [26] Lade PV, Duncan JM. Elastoplastic Stress-Strain Theory for Cohesionless Soil. Journal
601 of the Geotechnical Engineering Division 1975;101(10):1037-1053.
- 602 [27] Lade PV. Failure criterion for cross-anisotropic soils. Journal of geotechnical and
603 geoenvironmental engineering 2008;134(1):117-124.
- 604 [28] Sheng D, Sloan SW, Yu HS. Aspects of finite element implementation of critical state
605 models. Computational mechanics 2000;26(2):185-196.
- 606 [29] Ma C, Lu D, Du XL, Zhou AN. Developing a 3D elastoplastic constitutive model for soils:
607 A new approach based on characteristic stress. Computers and Geotechnics 2017;86:129-140.
- 608 [30] Gao ZW, Zhao JD, Li XS, Dafalias YF. A critical state sand plasticity model accounting
609 for fabric evolution. International journal for numerical and analytical methods in
610 geomechanics 2014;38(4):370-390.
- 611 [31] Xiong H, Nicot F, Yin ZY. A three - dimensional micromechanically based model.
612 International Journal for Numerical and Analytical Methods in Geomechanics 2017.
- 613 [32] Yu HS. CASM: A unified state parameter model for clay and sand. International Journal
614 for Numerical and Analytical Methods in Geomechanics 1998;22(8):621-653.
- 615 [33] Yu HS. Plasticity and geotechnics: Springer Science & Business Media; 2007.
- 616 [34] Rothenburg, L., Bathurst, R.J. Analytical study of induced anisotropy in idealized granular
617 materials. Géotechnique 1989; 39 (4). 601-614.
- 618 [35] Sitharam TG, Vinod JS, Ravishankar BV. Post-liquefaction undrained monotonic
619 behaviour of sands: experiments and DEM simulations. Géotechnique 2009; 59(9):739-49.
- 620 [36] Guo N, Zhao J.D. The signature of shear-induced anisotropy in granular media. Computer
621 and Geotechnics 2013; 47:1-15.
- 622 [37] Yu, H.-S. Non-coaxial theories of plasticity for granular materials. The 12th International
623 Conference of International Association for Computer Methods and Advances in
624 Geomechanics. Goa, India 2008.
- 625 [38] Schofield, A. and C. P. Wroth. Critical State Soil Mechanics. London, McGraw-Hill 1968.
- 626 [39] Been, K., et al. The critical state of sands. Géotechnique 1991; 41(3): 365-381.
- 627 [40] Wood, D. M. Soil behaviour and critical state soil mechanics. Cambridge University Press
628 1991.
- 629 [41] Ishihara, K. Liquefaction and flow failure during earthquakes. Géotechnique 1993; 43(3):
630 351-451.
- 631 [42] Hu N. On Fabric Tensor-based Constitutive Modelling of Granular Materials: Theory and
632 Numerical Implementation. PhD Thesis, University of Nottingham, 2015.

633 [43] Loukidis D, Salgado R. Modeling sand response using two-surface plasticity. *Computers*
634 *and Geotechnics* 2009;36(1):166-186.

635 [44] Itasca Consulting Group Inc.: PFC2D (Particle Flow Code in TwoDimensions). In. ICG,
636 Minneapolis, 1999.

637 [45] Haruyama, M. Anisotropic deformation-strength characteristics of an assembly of
638 spherical particles under three dimensional stresses. *Soils and Foundations* 1981; 21, 41-55.

639 [46] LADE, P. V. & ABELEV, A. V. Characterization of cross-anisotropic soil deposits from
640 isotropic compression tests. *Soils and Foundations* 2005; 45, 89-102.

641 [47] Li, X., H-S, Yu., X-S Li. A virtual experiment technique on the elementary behaviour of
642 granular materials with discrete element method. *International Journal for Numerical and*
643 *Analytical Methods in Geomechanics* 2013; 37: 75-96.

644 [48] Li, X., et al. Macro-micro relations in granular materials. *International Journal of Solids*
645 *and Structures* 2009; 46: 4331-4341.

646 [49] OCHIAI, H. & LADE, P. V. Three-dimensional behaviour of sand with anisotropic fabric.
647 *Journal of Geotechnical Engineering* 1983; 109, 1313-1328.

648 [50] Yang D.S. Microscopic Study of Granular Material Behaviours under General Stress Paths.
649 PhD Thesis, University of Nottingham, 2014.

650 [51] Ma, X., Zhang, D.Z. Statistics of particle interaction in dense granular material under
651 uniaxial compression. *J. Mech. Phys. Solids* 2006; 54, 1426–1448.

652 [52] Fu, P. and Y. F. Dafalias (2011). "Fabric evolution within shear bands of granular
653 materials and its relation to critical state theory." *International Journal for Numerical and*
654 *Analytical Methods in Geomechanics* 35(18): 1918-1948.

655